# Efficient, high-brightness soft-x-ray laser at 21.2 nm

B. Rus,* A. Carillon, P. Dhez, P. Jaeglé, G. Jamelot, A. Klisnick, M. Nantel,† and P. Zeitoun
*Laboratoire de Spectroscopie Atomique et Ionique, Université Paris–Sud, Bâtiment 350, 91405 Orsay Cedex, France*
(Received 1 July 1996)

In this paper we review the development of a soft-x-ray laser at 21.2 nm, recently carried out at the Laboratoire de Spectroscopie Atomique et Ionique. Amplification is generated by electron collisional pumping on a $2s^22p^53p$-$2s^22p^53s$, $J=0-1$ transition in neonlike zinc ($Zn^{20+}$). The lasing medium is a $\sim 150\ \mu m \times 2$ cm line plasma produced by irradiating slab Zn targets at a net intensity of $\sim 1.4 \times 10^{13}$ W cm$^{-2}$, using a 1.06-$\mu$m, 600-ps-long pulsed laser delivering $\sim 350$ J of net energy on the target. Accompanying the driving pulse by a 100-mJ-level prepulse train through deliberately imperfect isolation of the mode-locked laser oscillator, the $J=0-1$ gain coefficient $\sim 5$ cm$^{-1}$ is generated. The emission appears in an $\sim 100$-ps burst and precedes the lasing on both the much weaker $J=2-1$ lines and the x-ray continuum peak. The $J=0-1$ output source region, the beam spatial profile, and its time history have been measured and their relevance to the kinetics of this lasing system is discussed. A half cavity was implemented and a strong double-pass amplification at 21.2 nm with a 2-cm-long plasma obtained. With the gain-length product achieving $\sim 17.3$ according to the particular configuration, saturation was demonstrated, which is confirmed through a schematic model of the level kinetics. To our knowledge, it is the first neonlike soft-x-ray laser where saturation on the $J=0-1$ line was achieved by using a half-cavity arrangement. Absolute energy measurements indicate $\sim 400\ \mu J$ in the half-cavity-generated beam and a peak output power of $\sim 5$ MW, which makes this laser one of the most efficient soft-x-ray lasing systems demonstrated to date. [S1050-2947(97)01805-2]

PACS number(s): 42.55.Vc, 42.60.Da, 42.25.Kb, 52.50.Jm

## I. INTRODUCTION

The development of soft-x-ray lasers has been a subject of intense worldwide effort for more than a decade, following the initial demonstration of strong lasing near a wavelength of 20 nm [1]. Outstanding progress on many issues has especially been made recently [2–4]. Population inversion schemes by using ultrashort pulse drivers with the aim of obtaining lasing in the nanometer spectral region have been investigated [5–12]. The efficiency of the existing soft-x-ray lasers has been significantly improved [13–15] and x-ray beams of desired optical qualities have been produced [2,16–18]. Finally, a significant effort has been made on the development of applications of the soft-x-ray lasers [19,20].

While research on x-ray lasers emitting inside the water window and providing highly coherent beam is maintained by many laboratories, ultimately making possible the holography of living cells, there is a call for moderate- or small-scale devices supplying lasing action in the spectral region of tens of nanometers and being available to a wide scientific community. This need stems, on the one hand, from the prospect of many applications of such sources of extremely bright, coherent, and highly monochromatic radiation and, on the other hand, on the limited accessibility and low repetition rate of the present soft-x-ray lasers generated on large-scale facilities. The goal of this paper is to review the results of a program being undertaken at the Laboratoire de Spectroscopie Atomique et Ionique (LSAI) and the Laboratoire pour l'Utilisation des Lasers Intenses (LULI) on the development of a soft-x-ray laser emitting near 20 nm and addressing issues such as efficiency, feasibility, and repetition rate, which are crucial in the context of application research.

The soft-x-ray laser described uses collisional excitation pumping in neonlike zinc ($Z=30$). Its simplified Grotrian diagram representing levels involved in the observed lasing is shown in Fig. 1. Population inversions are produced at appropriate electron densities and temperatures between manifold $2p^53p$ and $2p^53s$ levels through a combination of electron collisional excitation from the Ne-like ground state $2p^6$ and dielectronic recombination from $F$-like states followed by radiative-collisional cascades. While the upper $3p$ levels are metastable with respect to radiative dipole decay to the ground, the lower $3s$ levels are strongly depleted by this process, which maintains the inversion. Among the $3p$-$3s$ fine-structure levels the strongest inversions are generated for the $(\frac{1}{2},\frac{1}{2})_{J=0} \rightarrow (\frac{1}{2},\frac{1}{2})_{J=1}$, and $(\frac{3}{2},\frac{3}{2})_{J=2} \rightarrow (\frac{3}{2},\frac{1}{2})_{J=1}$, and $(\frac{1}{2},\frac{3}{2})_{J=2} \rightarrow (\frac{1}{2},\frac{1}{2})_{J=1}$ transitions, using a $jj$-coupling description and notation $(j,j)_J$ referring to the angular momenta of the core and of the excited $3l$ electron, $J$ being the total angular momentum of the level. In this notation the real levels are labeled by the corresponding dominant pure $(jj)_J$ coupling:[1] the same applies to $LS$ notation; the use of which makes the above transitions to correspond for Zn XXI to $^1S_0 \rightarrow {}^1P_1$, $^1D_2 \rightarrow {}^3P_1$, and $^3P_2 \rightarrow {}^1P_1$. The wavelengths of these transitions of concern, henceforth abbreviated solely $J=0-1$ and $J=2-1$, are in

*Present address: Department of Gas Lasers, Institute of Physics, 18040 Prague 8, Czech Republic.
†Present address: Center for Ultrafast Optical Science, University of Michigan, Ann Arbor, MI 48109-099.

[1]In fact, each real state $JM$, where $M$ is the magnetic quantum number, is a linear superposition of $(jj)_{JM}$ eigenstates.

 

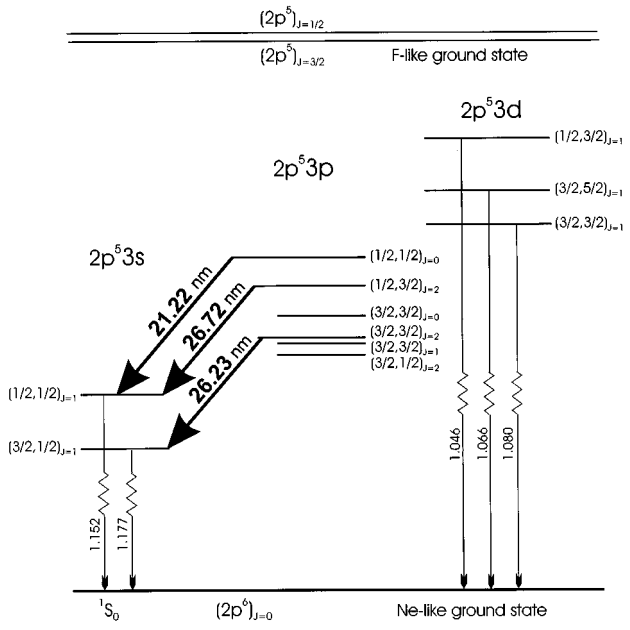


FIG. 1. Simplified Grotrian diagram of Ne-like zinc ($Z=30$). Among the $3s$ and $3p$ levels only those susceptible to provide lasing are shown (the wavelengths are labeled in nm). In addition to those indicated, population inversion may exist on the transitions $(\frac{3}{2},\frac{1}{2})_{J=2}\rightarrow(\frac{3}{2},\frac{1}{2})_{J=1}$, $(\frac{3}{2},\frac{3}{2})_{J=1}\rightarrow(\frac{3}{2},\frac{1}{2})_{J=1}$, $(\frac{3}{2},\frac{3}{2})_{J=0}\rightarrow(\frac{3}{2},\frac{1}{2})_{J=1}$, and $(\frac{1}{2},\frac{1}{2})_{J=0}\rightarrow(\frac{3}{2},\frac{1}{2})_{J=1}$ (''cross core''), providing wavelengths of 31.44, 27.86, 22.03, and 15.183 nm, respectively. Furthermore, amplification on the transition between core-excited levels $2s2p^63d(\frac{1}{2},\frac{5}{2})_{J=2}\rightarrow 2s2p^63p(\frac{1}{2},\frac{3}{2})_{J=1}$, corresponding to the wavelength of 22.69 nm [21], has been observed in this scheme in some experiments on Ne-like Ge [22,23].

neonlike zinc 21.22, 26.23, and 26.72 nm.

The collisional excitation scheme has proved to be the most robust approach to date for generating strongly amplified soft-x-ray radiation. The gain medium is usually a plasma column ablated from a massive slab target or a thin foil by impact of a laser pulse, and a bright x-ray beam is produced by amplified spontaneous emission (ASE). Using neonlike ions, intense soft-x-ray lasing has been demonstrated on elements ranging from Si ($Z=14$) to Ag ($Z=47$), supplying lines in a spectral range from 87.4 down to 9.9 nm [24–26], while by employing nickel-like ions wavelengths inside the water window (2.3–4.4 nm) have been generated [2]. Experimentally as well as theoretically the most extensively studied types from the those using neonlike sequence have been germanium ($Z=32$) and yttrium ($Z=39$) lasers (e.g., [2,27]), the former mainly due to a relatively modest required driving energy ($\sim$kJ), the latter rather for its high output power. The $Z$-scaling properties of the neonlike scheme, namely, a very strong $Z$ dependence of the necessary driving power and relatively slow scaling of the lasing wavelength, result in very poor efficiency in generating wavelengths in a nanometer spectral range, but, on the other hand, make this scheme suitable for producing strong lasing in the tens-of-nanometers region by using elements of a low atomic number. This has recently been shown the most spectacularly in a Ne-like argon ($Z=18$) laser emitting at 46.9 nm, which uses an alternative driving scheme based on capillary discharge [4] and approaches a ''table-top'' size. The efficiency of this scaling is also clearly demonstrated in the present work where gain lengths $\sim 10$ in single pass ASE at 21.2 nm are obtained using only a $\sim$430-J driver.

Despite the successful implementation of the neonlike collisional scheme, some issues are not yet fully understood. Although detailed numerical modeling predicts the strongest gain for the $(\frac{1}{2},\frac{1}{2})_{J=0}$ to $(\frac{1}{2},\frac{1}{2})_{J=1}$ transition, as a consequence of the high rate of monopole collisional excitation of the $(\frac{1}{2},\frac{1}{2})_{J=0}$ level from the ground under appropriate densities, experimentally the $J=2-1$ lasing lines have been found to dominate the output of these systems when driven by a single pulse. The main reasons likely for this discrepancy may lie in the inaccurate treatment of the $(\frac{1}{2},\frac{1}{2})_{J=0}$ level in atomic physics calculations, which constitutes an independent research topic [28,29], and/or in inaccurate modeling of the plasma profile near the critical surface where the $J=0-1$ gain is generated, especially in the early plasma times.

Recently it has been revealed that the $J=0-1$ output from slab-target systems may be greatly promoted by techniques consisting basically, albeit not exclusively, in the alleviation of plasma refraction. This is accomplished by applying a weak prepulse several nanoseconds prior to the main driving pulse [30–33] or by using a sequence of two or three laser pulses [34,35]. While these approaches have very recently become quite widespread, it should be underlined that the full quantitative understanding of the effects involving prepulsed pumping using very weak irradiance is still presently incomplete despite the experimental [36–39] and theoretical [40,41] progress achieved. Another technique for boosting the $J=0-1$ output is using bent targets [42], where refraction is compensated by gain region curvature, which may be employed in conjunction with the prepulse or the sequential pumping regime [43,44].

The strong $J=0-1$ lasing in the zinc laser described is achieved through small-level prepulse pumping, with prepulses containing $\sim 5\times 10^{-4}$ of the energy of the main driving pulse and producing target irradiance of order $7\times 10^9$ W cm$^{-2}$. Although high gain at 21.2 nm has been reported [45], the key role of extremely weak prepulses for this laser was not quantitatively recognized until later. The prepulse technique as a means to greatly boost the $J=0-1$ output in neonlike systems has been known since 1993 [30,31] using typically 6-J prepulses to produce $\sim 2\times 10^{11}$ W cm$^{-2}$ on the target, at a level of $\sim 5\times 10^{-3}$ with respect to the main pulse. The intense lasing at 21.2 nm reported in [45] was, however, due to prepulses remnant in the shot from the mode-locked laser oscillator, which were at a much lower level and were undetectable by then available techniques monitoring the parameters of the LULI laser shot. Following the results by Cairns *et al.* [32,33] showing that a significant effect could be produced in neonlike germanium with a prepulse level as low as $\sim 2\times 10^{-4}$, a modification was made in the LULI laser chain so as to produce prepulse-free pulses. This allowed us to establish the role of the prepulses in our $J=0-1$ Zn laser [13,46]. The sensitivity of the $J=0-1$ line in neonlike Zn to very weak prepulses was also independently demonstrated in [47].

The 21.2-nm zinc laser described here uses a pumping sequence consisting of a train of prepulses now controllably

produced as a remnant from the laser oscillator. The basic differences in the performance of the laser with and without the prepulses are presented and discussed in this work. While still being pursued, a detailed investigation of the dependence of the 21.2-nm output on the individual prepulse parameters such as contrast or timing with respect to the driving pulse has been made and its results are discussed elsewhere [36–38,48].

An important part of our work concerns experiments on double-pass amplification using a half cavity. This arrangement is known to have a high potential of enhancing the total x-ray laser output and hence the efficiency of the system as well as of improving optical qualities of the x-ray beam. However, difficulties with its implementation have been reported in a number of experiments. More specifically, the half-cavity mirror was destroyed in some cases before conditions for significant amplification were created in the plasma (see, e.g., [2,49]). The maximum distance of the mirror from the plasma end being dictated by the duration of gain phase, the mirror survival in the particular conditions is a critical issue for the success of such experiments. In this work an efficient half-cavity operation is demonstrated with a mirror placed at a distance as short as 6 mm. We discuss various aspects relevant to the half-cavity operation and outline issues connected to its practical design making it possible to routinely perform half-cavity shots with a single mirror alignment.

By using half-cavity saturated output at 21.2 nm was produced. Temporal and spatial characteristics of the emitted x-ray beam were measured and a brief account of the obtained results is presented. The absolute measurements of the beam energy allows one to evaluate the performance of the laser in terms such as instantaneous power and brightness and to compare it with other laboratory soft-x-ray sources available.

The paper is structured as follows. Section II describes the experimental conditions under which this work was made and the x-ray diagnostics employed. The results of measurements of various characteristics of the single-pass $J=0-1$ ASE output at 21.2 nm are presented in Sec. III and are compared to the analogous parameters of the $J=2-1$ lines. In Sec. IV we discuss some aspects of the half-cavity design and in Sec. V the obtained results of double-pass amplification at 21.2 nm are presented. The experimental data are accompanied by results of a schematic modeling confirming that saturation is achieved. Section VI concludes and outlines prospects for application of this soft-x-laser being currently in progress or to be developed in the future.

## II. EXPERIMENTAL ARRANGEMENT

The experiments were conducted at the x-ray laser facility of the LULI at the École Polytechnique, Palaiseau, France. The plasma is created by irradiating flat zinc slabs 2 cm in length by six 90-mm-diam beams of the LULI Nd:glass laser. Energies typically 430 J at the fundamental wavelength of 1.06 $\mu$m are available for these experiments at the output of the laser, in near-Gaussian $\sim$600-ps full width at half maximum (FWHM) pulses. Each laser beam is focused down to a line $\sim$2.4 cm long and $\sim$100 $\mu$m wide by a pair of $f/7.4$ and $f/10$ crossed cylindrical lenses. The line foci

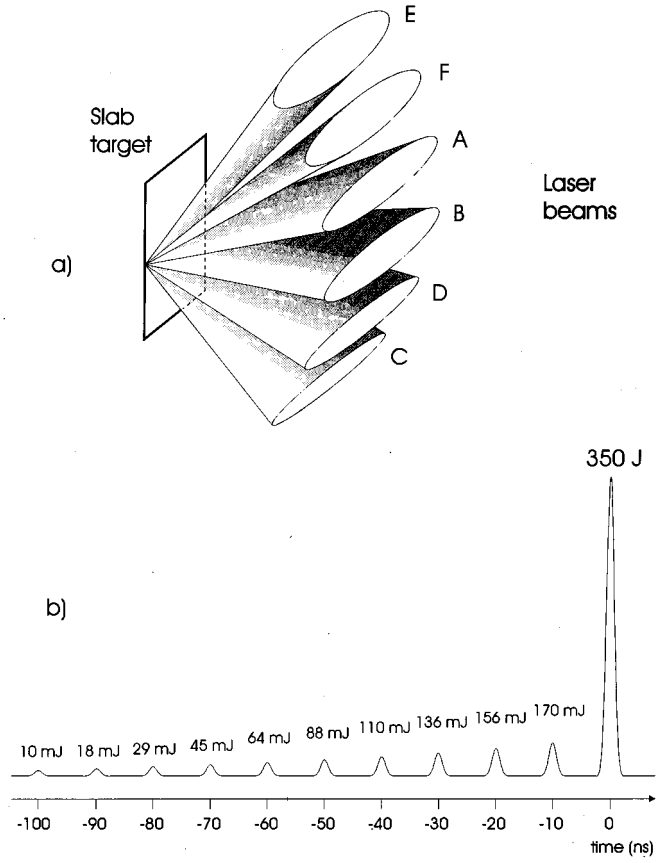


FIG. 2. (a) Target irradiation geometry at the XRL facility at LULI. The laser beams arrive separated by 18° in the vertical plane; the total angle between extreme beams is thus 90°. (b) Temporal structure of the LULI laser pulse (not to scale). The main driving pulse is preceded by a train of small prepulses separated by 10 ns. All the values indicated correspond to the net total energy on the target; those belonging to the prepulses are measured with a precision of about 50%. The last prepulse in the train to the main pulse energy ratio is $5(\pm 2)\times 10^{-4}$.

thus generated are superimposed upon one another [see Fig. 2(a)] with a precision greater than 50 $\mu$m, giving rise to the resulting spot $\sim$150 $\mu$m wide and creating a net target irradiance typically $\approx 1.4\times 10^{13}$ W cm$^{-2}$. Slightly overfilling the 2-cm-long target by the 2.4-cm line focus avoids creation of a cold plasma at the target ends. Good irradiation uniformity along the focus axis is ensured primarily by the radial profile of the laser beams with the intensity near the circumference being typically $\approx$50% higher than the intensity on the axis, which is generated by the rod-based LULI laser in the absence of some of the apodizers in the chain. With appropriate focusing a considerably more uniform intensity distribution along the focal line may thus be generated, in contrast to a beam of flat profile.

A parameter of fundamental importance in the functioning of the soft-x-ray laser under investigation is the employed temporal structure of the pumping laser. The main laser pulse driving the highly ionized plasma is accompanied by a train of small pulses separated by 10 ns, as schematically shown in Fig. 2(b). The train is a remnant from the mode-locked laser oscillator, which is intentionally imperfectly isolated by operating only one Pockels cell in the

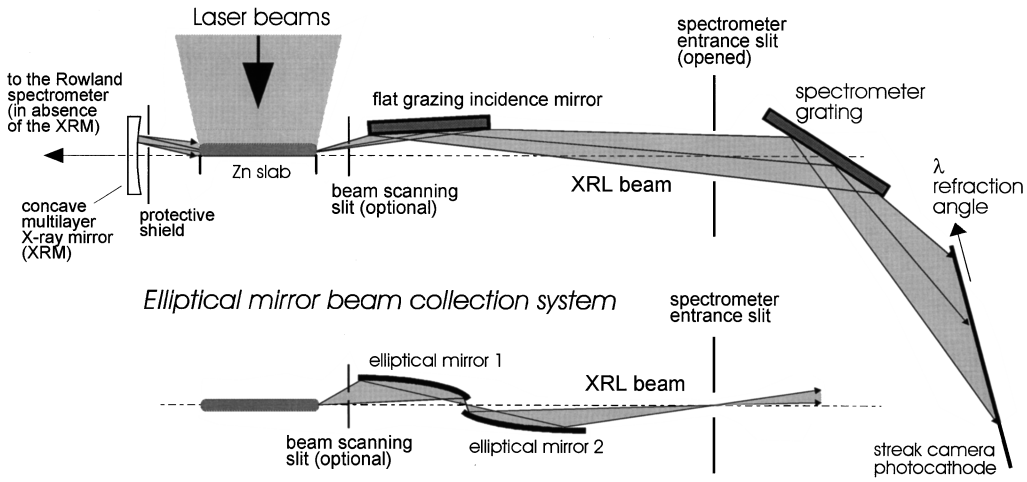


FIG. 3. Experimental setup for investigation of collisionally pumped XRL at LULI. The Focal spectrometer (see the text) is converted into an analyzer of XRL beam divergence with the help of a plane mirror, whereas the elliptical mirror system covering refraction angles of 0–15 mrad collects the total XRL emission produced and is used in gain measurements. The axial soft-x-ray emission emerging westward is analyzed by the Rowland spectrometer (not represented here), while the half-cavity multilayer mirror protected by a pierced shield is placed on this side of plasma in the double-pass amplification shots.

chain. The last prepulse preceding the main pulse delivers $\sim 170$ mJ of energy on the target and produces a net irradiance $\approx 7\times 10^{9}$ W cm$^{-2}$. The overall energy of all the prepulses preceding the main driving pulse is about 800 mJ.

A scheme of the basic arrangement of the target and the diagnostics being used throughout this work is shown in Fig. 3. The targets employed are 1-mm-thick zinc plates of a purity 99.99+%, mechanically polished to a surface flatness better than $\sim 50$ $\mu$m. After each shot the target is vertically translated by typically 300 $\mu$m and the plate height of typically 7 cm allows it to be used it for more than 100 shots.

The soft-x-ray emission emerging near the plasma axis is on the east side detected by the Focal grating spectrometer coupled to a streak camera and on the west side by the Rowland spectrometer providing time-integrated data. The Focal spectrometer [50] has been used in these studies as the principal instrument for analyzing the emitted soft-x-ray spectra. It employs Wadsworth geometry in which parallel emission of a given direction is focused to a point on the focal circle and uses a blazed spherical grating with 900 lines/mm as a dispersive element. It provides a viewing field of roughly 20 Å, with a resolution of $\sim 0.7$ Å, in a spectral range between about 40 and 700 Å. The Kentech Low Magnification x-ray streak camera using a reflective photocathode and having a time resolution of order 10 ps is used as the detector. The spectrometer was adapted for use in experiments on collisional excitation x-ray lasers by adding beam collection optics that reflects the off-axis refracted x-ray emission towards the entrance slit. There are two devices used alternatively: an elliptical mirror system serving to gather the total x-ray laser emission and a plane mirror that is used for a precise analysis of the x-ray laser beam in a limited range of refraction angles. In the elliptical mirror system two glass plates are bent to elliptical shape in a matrix and are arranged in such a way that two of their focal points are matched while the other two correspond respectively to the target edge and the spectrometer entrance plane (see Fig. 3). The arrangement covering refraction angles up to 15 mrad thus produces perfect imagery between the pair of conjugate axial points corresponding to their two distant foci while working as an optical system with transverse magnification of about 12 for near-axis objects. The reflected emission enters the spectrometer slit under an angle about 10 times smaller than its refraction angle and consequently appears shifted in wavelength on the detector plane, with respect to its nominal position corresponding to the axial direction. Ray tracing [48] reveals that due to astigmatic properties of the system as well as due to alignment imprecision and assumed fabrication imperfections, the emission emerging from an $\sim 100$-$\mu$m region at the plasma exit plane is spread out over $\sim 3$ mm at the slit plane, which determines a requirement for the slit width.

The 20-cm-long plane mirror is a nonfocusing element and is employed with the spectrometer entrance slit open. The arrangement thus works with very small spectral resolution capability and is designed to analyze quasimonochromatic emission with respect to the spectrometer viewing window, as is the case of the investigated soft-x-ray laser emission. Individual rays are incident on the grating under different angles and each point at the streak photocathode thus corresponds to a particular ray direction, i.e., to a particular refraction angle. In a typical setup for measuring the angular characteristics of the 21.2-nm beam the mirror covers refraction angles ranging from $\sim 5.5$ to $\sim 10$ mrad.

In experiments on single-pass ASE the west-going axial soft-x-ray emission is analyzed by the Rowland spectrometer [51] using a 3600-lines/mm blazed spherical grating and making it possible to record in a single shot a wavelength window of $\sim 20$ nm, with a high resolution $\Delta\lambda/\lambda$ of $\sim 5\times 10^{-4}$. Time-integrated spectra are recorded using $\sim 18$-cm-long Kodak SC5 XUV flexible film plates attached to the Rowland circle by a bending jig. The x-ray emission is brought to the spectrometer entrance slit by a pair of two grazing incidence toric mirrors working as an imaging system in the tangential (i.e., horizontal) plane. The angular acceptance of this system is roughly 15 mrad.

Although not shown in Fig. 3, a standard diagnostic device used in all experiments were a multipinhole camera [52]

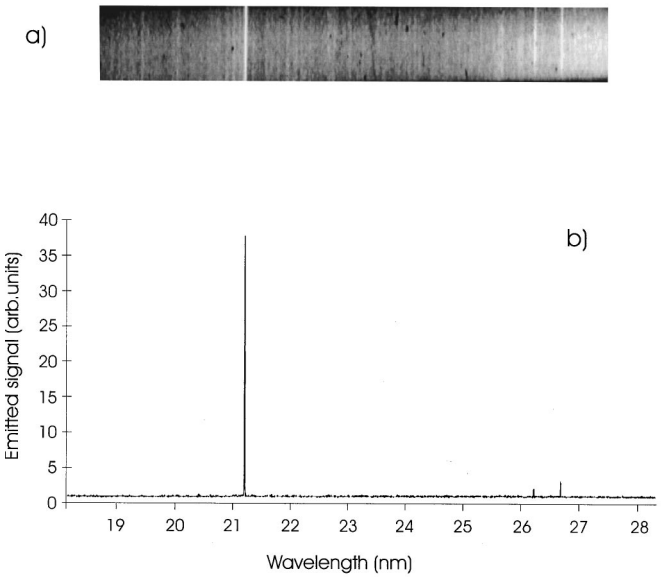


FIG. 4. (a) Time-integrated film record of soft-x-ray axial spectrum emitted by a 2-cm plasma, obtained with the Rowland spectrometer, covering a spectral range $\sim 18-28$ nm. (b) Emitted time-integrated axial spectrum obtained from (a) by converting the exposed film optical density into the incident intensity. The $J=0-1$ lasing line at 21.2 nm entirely dominates over two weaker $J=2-1$ lines at 26.2 and 26.7 nm.

with a charge coupled device (CCD) detector, providing a front view of the plasma keV emission and supplying thus information both about the plasma lateral width and its uniformity. This information is, among other things, used to indicate that similar target irradiating conditions are achieved in successive laser shots, as well as in different experimental sessions.

In some of the experiments a flat-KAP-crystal imaging spectrometer was employed to record the $L$-shell resonance lines, providing spatial resolution along the plasma axis. The keV time-integrated spectra thus acquired made it possible to survey the plasma ionization balance and its uniformity along the axis and served to infer the electron temperature and Ne-like ground-state density as well as the lateral size of the Ne-like region. While we briefly mention some of the results in this paper, we do not discuss them as they constitute an independent topic and have been described in detail elsewhere [36,37].

Besides this basic diagnostic suite, several simple devices were employed in some measurements. Their brief description will be given along with the obtained results. The arrangement of the half cavity and its design will be described separately in Sec. IV.

## III. CHARACTERISTICS OF THE $J=0-1$ SINGLE-PASS ASE AT 21.2 nm

Except where explicitly noted, the data presented in this paper were obtained with the nominal driving conditions, i.e., at a net target irradiance of $\sim 1.4\times 10^{13}$ W cm$^{-2}$ and with the prepulse train of parameters displayed in Fig. 2(b). Figure 4 illustrates a typical large-band time-integrated axial spectrum from a 2-cm-long Zn plasma, obtained with the Rowland spectrometer. The film record covers a spectral range from about 18 to 28.3 nm. The $J=0-1$ lasing line at 21.2 nm dominates the spectrum, with time-integrated intensity exceeding about 15 times the intensity of the $J=2-1$ lines. No amplification is seen on the other two potentially lasing $3p$-$3s$ transitions falling into this spectral window, namely, $(\frac{3}{2},\frac{3}{2})_{J=0}$ to $(\frac{3}{2},\frac{1}{2})_{J=1}$ at 22.03 nm and $(\frac{3}{2},\frac{3}{2})_{J=1}$ to $(\frac{3}{2},\frac{1}{2})_{J=1}$ at 27.86 nm, and on the $(2s2p^6 3d)_{J=2}$ to $(2s2p^6 3p)_{J=1}$ inner-shell hole transition at 22.69 nm.

Figure 5(a) shows a typical example of the streak record of the 21.2-nm emission from a 2-cm plasma, obtained by using the Focal spectrometer and the elliptical mirror system. The emission appears in a short burst $\approx 100$ ps and exhibits a strongly pronounced maximum. These characteristics are observed to be fairly independent of the plasma length, although the intensity strongly increases with plasma lengthening.

The crucial role of the prepulses in the generation of the strong $J=0-1$ lasing is illustrated in Fig. 5(b), displaying temporal evolution of the 21.2-nm output from a 2-cm plasma in two different pumping modes. While the first plot corresponds to the streak data shown in Fig. 5(a) when the nominal prepulse train with the fractional intensity $\approx 5\times 10^{-4}$ of the last prepulse to the main pulse of intensity $\sim 1.4\times 10^{13}$ W cm$^{-2}$ is applied, the second plot corresponds to the case when only the heating pulse of otherwise identical parameters drives the plasma. More specifically, in the latter case the prepulse energy was reduced by a factor of $\sim 700$, i.e., the irradiance corresponding to the intensity of the last prepulse in the train to $\sim 10^7$ W cm$^{-2}$, by switching an additional Pockels cell behind the first preamplifier in the laser chain. The result of this comparison is clear: the 21.2-nm output virtually disappears when the prepulse train is absent, being barely discernible from the background, and is at least 30 times less intense than when the prepulse train is applied.

Figure 6 represents the 21.2-nm temporal peak intensity, spectrally integrated over the line profile, as a function of the plasma length. It should be noted that the data, obtained in an accurate measurement devoted to the intensity vs plasma length dependence, exhibit a very good exponentiation. The measured values are fitted to the Linford function [53], expressing the intensity produced by an ASE system of length $l$,

$$I(l)=w\,\frac{j}{g}\,\frac{[\exp(gl)-1]^{3/2}}{\sqrt{gl\,\exp(gl)}}, \tag{1}$$

where $j$ is the spectral peak emissivity, $g$ the spectral peak gain coefficient, and $w$ a factor depending on the intrinsic line profile. The best least-squares fit to the data yields a gain of $4.9\pm 0.2$ cm$^{-1}$ and is represented in Fig. 6 as a solid curve. The value of 4.9 cm$^{-1}$, implying a gain-length product of $\sim 9.8$ for the 2-cm plasma, is used throughout this work as a nominal one for evaluating some other characteristics of the 21.2-nm emission, inasmuch as rough measurements carried out, under identical driving conditions, on other occasions provided very similar values.

The gain coefficient on the $J=2-1$ lasing lines at 26.2 and 26.7 nm was measured to be $2.3\pm 0.6$ and $2.6\pm 0.4$ cm$^{-1}$, respectively [45]. More importantly, the $J$

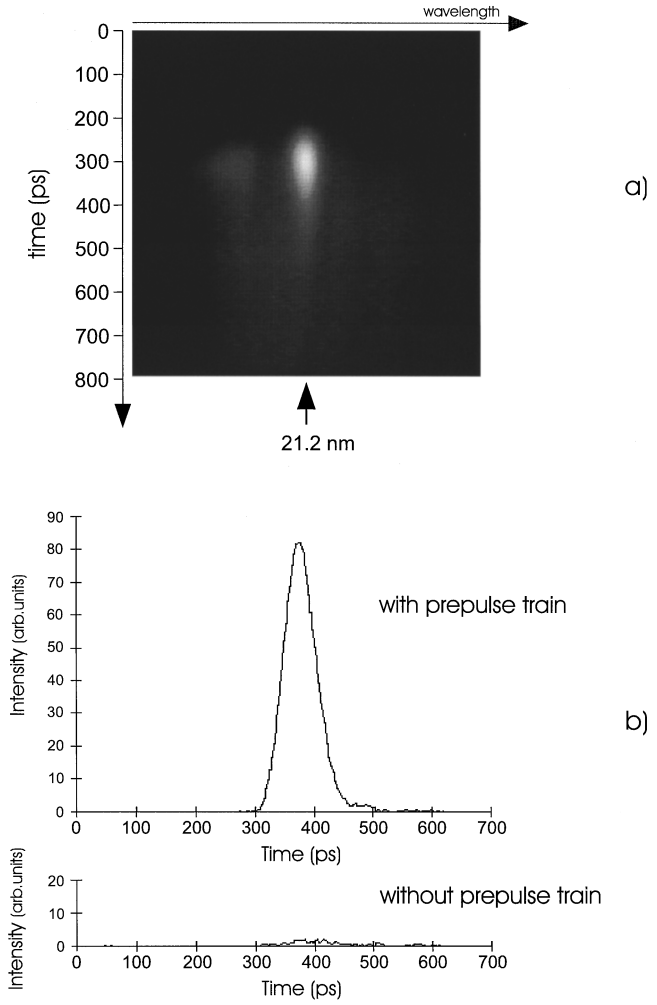


FIG. 5. (a) Streak record of the $J=0-1$, 21.2-nm emission produced by a 2-cm plasma, obtained with the help of the elliptical mirror system. (b) Comparison of the $J=0-1$ output from a 2-cm plasma when the nominal prepulse pumping [see Fig. 2(b)] is used and when only a single driving pulse is employed (the prepulse train is reduced in this case by a factor of $\sim 700$ by using additional Pockels cell in the laser chain).

$=2-1$ output has been observed to be almost insensitive to the presence of the prepulse train, in strong contrast to the $J=0-1$ case.

The time history of the lasing lines emitted by a 2-cm plasma is plotted in Fig. 7. Two streak records, corresponding to the $J=0-1$ and $J=2-1$ measurements, are mutually timed with the help of the soft-x-ray continuum with a precision $\approx \pm 50$ ps. The $J=0-1$ emission peaks $100 \pm 50$ ps before the $J=2-1$ lines that roughly follow the evolution of the continuum, the maximum of which is expected to occur near the peak of the driving laser pulse. The FWHM duration of the $J=0-1$ signal is $\approx 100$ ps which is noticeably shorter than the $\sim 300$-ps duration of the $J=2-1$ emissions. The behavior represented in Fig. 7 was observed to be weakly sensitive on both the driving laser energy and the plasma length.

The occurrence of the ASE signal at 21.2 nm in early plasma times and its short duration clearly indicates that the $J=0-1$ inversion is predominantly driven by processes other than the $J=2-1$ inversions and that the corresponding

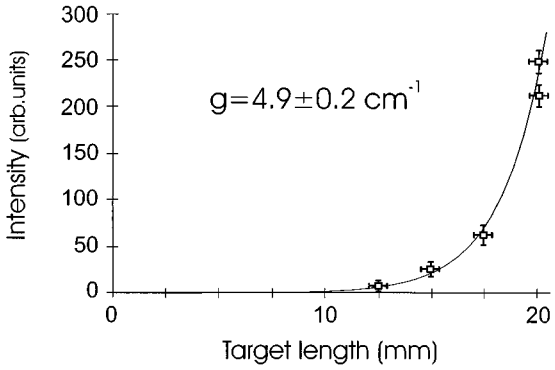


FIG. 6. The 21.2-nm peak intensity vs plasma length. The solid curve is the Linford fitted function corresponding to a gain coefficient of 4.9 $cm^{-1}$.

x-ray beams are subject to different propagation conditions in the plasma. A quantitative analysis of the streak data from different plasma lengths suggests [45,48] that the temporal structure of the $J=0-1$ output is governed by the evolution of the emissivity rather than by the evolution of the gain: the analysis shows the latter to exhibit little variation from $-50$ to $+150$ ps relative to the ASE output. Another conclusion, allowing for the fact that the $J=0-1$ and 2–1 transitions at 21.2 and 26.7 nm share the same lower level $(\frac{1}{2},\frac{1}{2})_{J=1}$, was that these lines come from different plasma regions. This was confirmed by a direct measurement of the near-field ASE pattern, carried out with the help of a simple device consisting of a precisely positioned stainless cut edge placed 1 mm from the plasma end at the Focal spectrometer side. The edge was advanced in each shot by steps 25 $\mu$m away from the target surface to gradually screen the emitting region and the desired information was obtained by subtracting the signals received in two subsequent positions of the edge. The drive beams were carefully apertured so that no laser light hit and ablated the edge. The obtained results for a 2-cm plasma are shown in Fig. 8. It is seen that the 21.2-nm emission emerges essentially from a narrow $\sim 35$-$\mu$m (FWHM) region strongly peaked $\approx 30$ $\mu$m from the target surface, whereas the 26.7-nm line is emitted over an $\sim 200$-$\mu$m broad zone and its maximum appears at a distance $\approx 100$ $\mu$m. The strong dominance of the $J=0-1$ emission near the target, i.e., in a high-density plasma, suggests once again the collisional pumping to be the major process populating the $J=0$ upper level.

The results of the far-field pattern measurement of the $J=0-1$ ASE are shown in Fig. 9(a), which displays angular profiles of the 21.2-nm beam produced by a 2-cm plasma, corresponding to times separated by 50 ps with respect to the instant of the emission peak (the streak data are also included). It is seen that the beam is very narrow with a divergence at the instant of its maximum of $2.8 \pm 0.5$ mrad. The refraction angle quickly diminishes early in time and stabilizes at $7.2 \pm 0.5$ mrad starting from the emission temporal peak. The 21.2-nm beam divergence undergoes only a minor evolution, but slightly increases as time progresses. The characteristics of the $J=2-1$ beams were revealed to strongly differ from those of the $J=0-1$ beam. Data for the $J=2-1$, 26.7-nm emission corresponding to the instant of its maximum are shown in Fig. 9(b). They provide a fairly flat

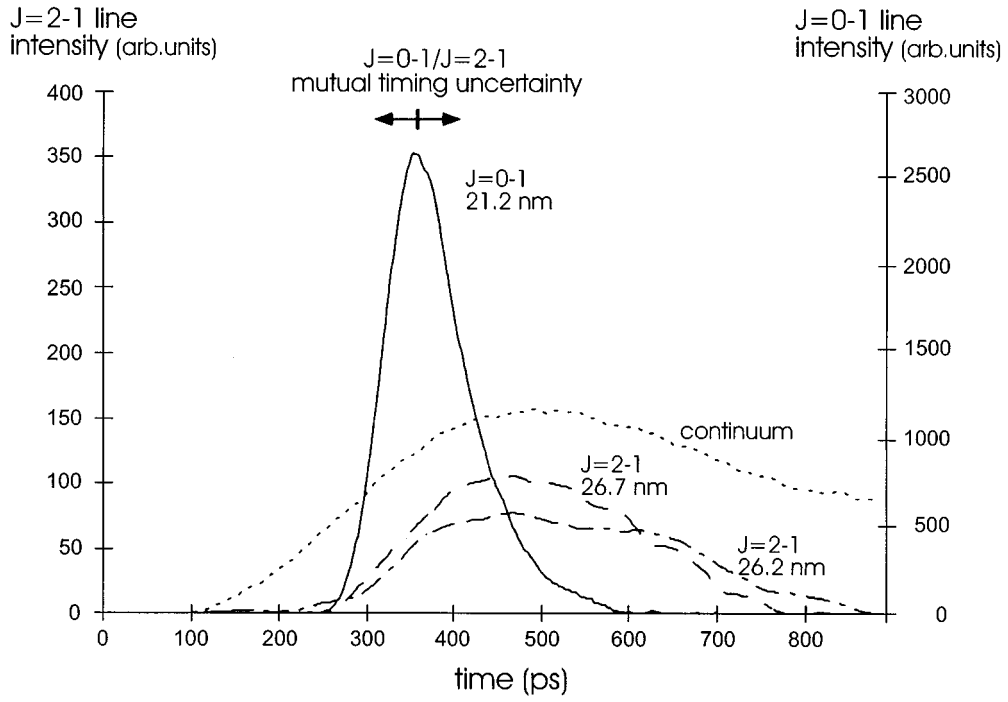


FIG. 7. Time evolution of the lasing lines and the soft-x-ray continuum (dashed curve, not to scale) emitted by a 2-cm plasma. Note different vertical scales for the $J=0-1$ and $J=2-1$ lines. It is apparent that conditions for the strongest $J=0-1$ amplification occur before those leading to maximization of the $J=2-1$ lines, as well as before the peak of the continuum emission, which is expected to maximize near the peak of the driving laser pulse.

beam profile with a divergence of $11\pm4$ mrad, peaking $15\pm3$ mrad off axis. Almost identical characteristics were measured for the $J=2-1$, 26.2-nm beam.

In addition to the basic importance of the $J=0-1$ beam characteristics for development of the half cavity, these data, along with the measured near-field profiles, supply valuable information about the density and the gain region profiles. First, whereas the $J=0-1$ emission emerges from the 2-cm plasma as a strongly collimated beam, the divergence of the $J=2-1$ beams is much larger [the value 11 mrad roughly corresponds to the gain region aspect ratio; see Fig. 8(b)]. This indicates that while a number of rays propagating along different trajectories experience comparable gain in the case of the $J=2-1$ emission, a narrowly defined optimal ray path producing maximal amplification exists for the $J=0-1$ emission.

Second, the $J=0-1$ beam is seen to be significantly less refracted than the $J=2-1$ beams although it emerges from denser plasma. In the subcritical plasma with a scale length $L$ the local refraction ratio scales as $d\alpha/dz\propto\lambda^2 n_e/L$, where $\alpha$ is the ray angle with respect to the longitudinal axis $z$ and $n_e$ is the electron density. Despite its shorter wavelength, the $J=0-1$ beam should thus be expected to be more refracted than the $J=2-1$ beams as it is generated in an active region located principally in high-density plasma.

Ray tracing simulations have been performed to help understand these observations [48,54]. This modeling reveals that in a plasma profile with a density scale length below 100 $\mu$m, typical for a single-pulse driving by an intensity $\approx1.4\times10^{13}$ W cm$^{-2}$ (e.g., [55]), the $J=0-1$ emission would suffer severe refraction and could in no case receive amplification in the narrow gain region along the full 2-cm plasma length. No near exponential growth with respect to plasma length would be possible in such a case, in strong contrast to the observed intensity vs length exponentiation as shown in Fig. 6. On the other hand, the measured near-field $J=0-1$ intensity profile and the near exponential behavior may be theoretically reproduced, assuming a relaxed electron density profile characterized by a scale length of about 125 $\mu$m, which is 2–3 times larger than values occurring in a single-pulse-driven plasma. The major finding discussed in detail in [54] is that in the large-scale length plasma the $J=0-1$ emission receives maximal amplification only along a well-defined, roughly symmetrical trajectory remaining within the narrowly peaked gain region. In contrast, in the broad and rather uniform $J=2-1$ active region with a smaller local gain at lower densities there exist many ray paths producing comparable gain lengths, though the maximal amplification occurs for a ray that begins in dense plasma, thus benefiting from high spontaneous emission, and propagates along the gain region to be almost refracted out of it at the exit. This results in a beam profile refracted more strongly than the $J=0-1$ beam and having a significantly larger divergence, as observed experimentally.

The fact that the prepulsed pumping used significantly increases the plasma scale length appears to be further supported by the pinhole camera images of the plasma in the keV spectral region, shown in Fig. 10. We see that in the prepulse regime the lateral plasma dimension is $\sim60\%$ greater than in the single-pulse driving, which indicates that the lateral (vertical) refraction is alleviated through this plasma profile broadening, and also suggests that comparable scale length augmentation may be expected in the transverse direction. Furthermore, it is seen that the plasma created in the prepulse regime emits more intensely in the keV region and that its uniformity along the axis is improved. The higher intensity of the keV radiation suggests the plasma is denser and/or more spread (voluminous) in the direction perpendicular to the target, which are both modifications acting toward enhancement of the $J=0-1$ laser output. We note that a detailed study of the parameters of the zinc plasma, carried out through a keV line spectroscopy [36,37], con-

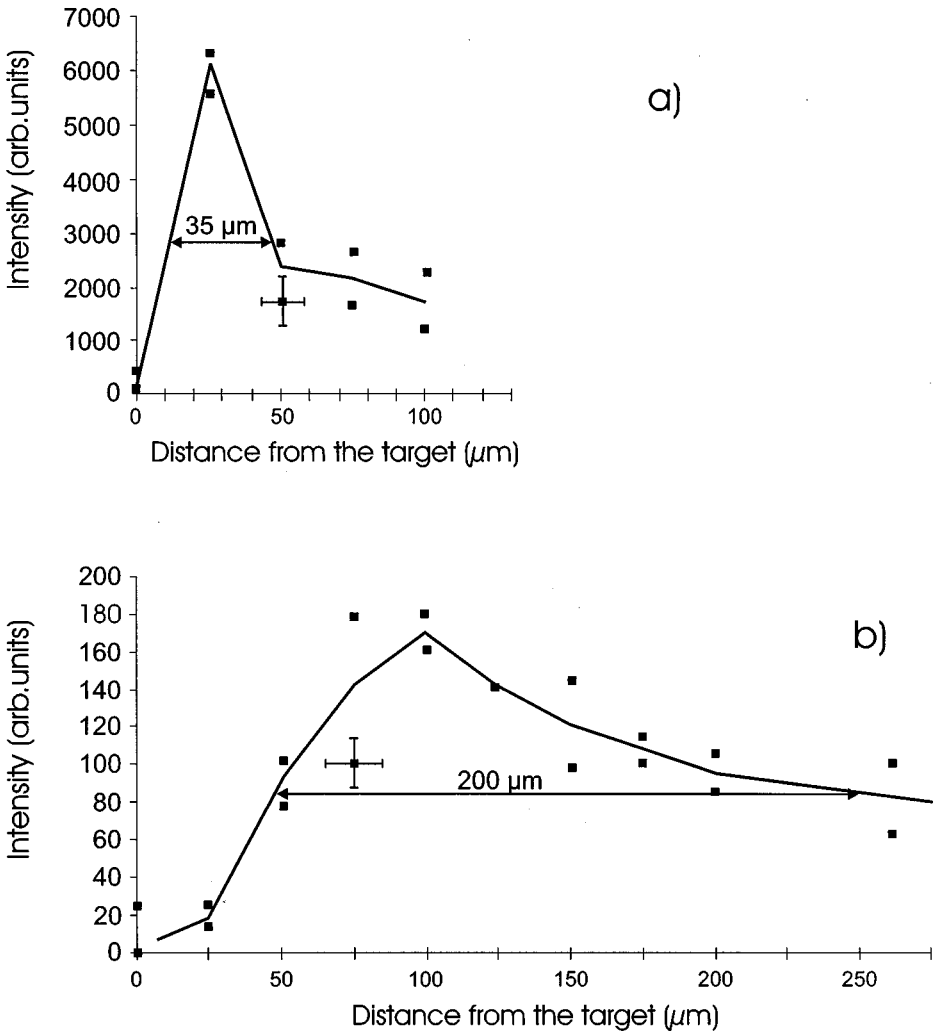


FIG. 8. Distribution of the intensity of the (a) $J=0-1$, 21.2-nm emission and (b) $J=2-1$, 26.7-nm emission at a plane 1 mm away from the exit of a 2-cm-long plasma. The data were obtained by scanning this plane by a precisely positioned cut edge; the accuracy of this positioning with respect to the target surface was better than $\pm 10\ \mu$m. The points correspond to the distances intermediate between two subsequent positions of the edge. Two sets of shots for each line were carried out so as to establish the shot-to-shot reproducibility.

firms the aforementioned observations by measuring an $\sim 50\%$ increase of the lateral plasma dimension and an $\sim 30\%$ increase of the Ne-like ground-state density when the prepulse train pumping is applied.

## IV. HALF-CAVITY DESIGN FOR ACHIEVING DOUBLE-PASS AMPLIFICATION AT 21.2 nm

The results obtained in single-pass ASE regime allowed us to proceed to the development of a half cavity, with the aim of significantly boosting the output power—and in turn improving the efficiency—of this soft-x-ray laser, as well as generating a bright, narrowly collimated 21.2-nm beam with a high degree of coherence. An x-ray mirror (XRM) placed near one end of the plasma provides an optical feedback, the magnitude of which we define as the fraction of the intensity of the ASE beam, returned to the gain region for reamplification. Referred to henceforth as effective reflectivity $R_{\mathrm{eff}}$, it may be expressed as

$$R_{\mathrm{eff}}=RC_g, \tag{2}$$

where $R$ is the normal-incidence reflectivity of the mirror and $C_g$ the geometric coupling efficiency, accounting for the reflected beam geometric overlap with the gain region at the plasma entrance plane. The value of $C_g$ depends solely on the XRM geometry, on the gain region dimensions, and on the parameters of the x-ray beam and may be easily calculated with the help of ray optics (for details see [13,48]). On the other hand, endurance of the reflectivity $R$ during the event may be established exclusively by the experiment, in particular from the temporal evolution of the half-cavity output as an eventual sudden loss of reflectivity would bring about a rapid alteration of the emitted signal (e.g., [49]). This is due to the fact that a complete understanding of mechanisms responsible for the structural damage of a multilayer structure in the laser plasma environment is yet to be achieved, although plasma x-ray radiation and side-scattered stimulated Brillouin scattering have been identified as the predominant causes [2]. In this work the XRM survival during the x-ray pulse duration is apparent from the data presented in Sec. V.

The ratio of the output x-ray laser intensity $I_{\mathrm{XRM}}$ generated by the half cavity and the single-pass ASE intensity $I$ may be, in the nonsaturated regime, evaluated by using Eq. (1). Labeling $g_f$ and $g_r$ the gain coefficients relevant, respectively, to the forward and the return propagation of the x-ray beam through the plasma, the ratio of the intensities in the unsaturated regime will be

$$\frac{I_{\mathrm{XRM}}}{I}=R_{\mathrm{eff}}\left(1+\frac{g_r}{g_f}\right)^{-1/2}\exp(g_r l), \tag{3}$$

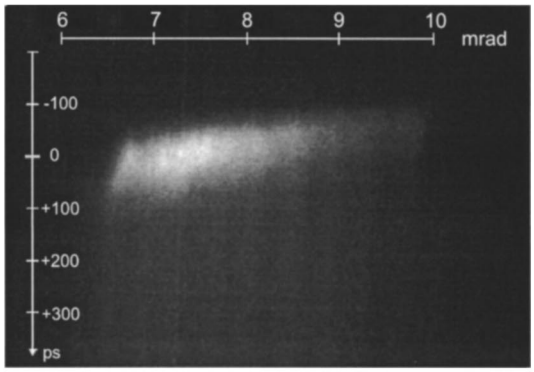


a)

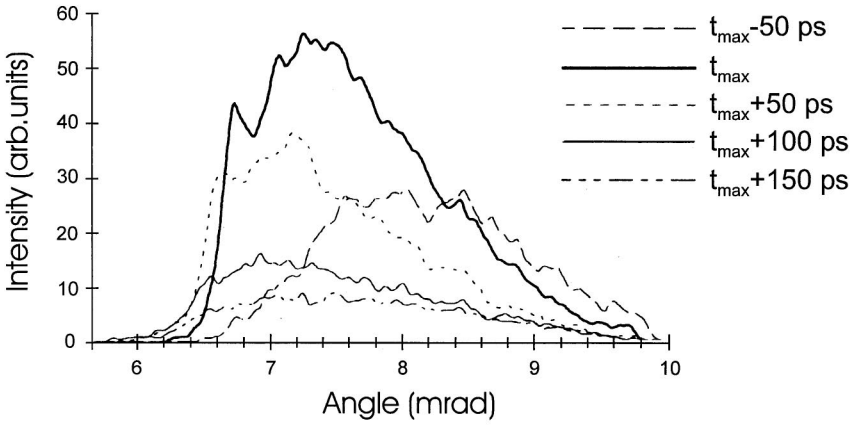


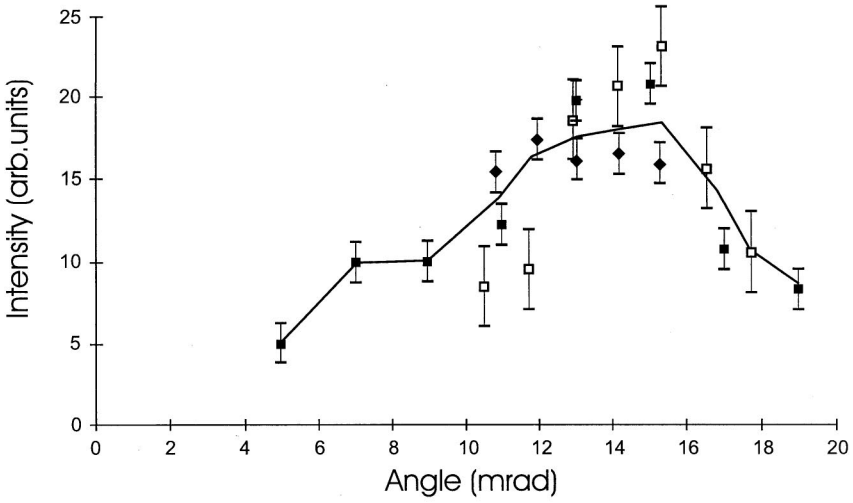


b)

FIG. 9. (a) Angular profile of the 21.2-nm beam emitted by a 2-cm plasma, in instants separated by 50 ps with respect to its maximum. It is seen that the beam peaks at $\sim 7.2$ mrad off axis and its divergence is $\sim 2.8$ mrad. The data were obtained using the plane mirror; the corresponding raw streak record is also shown. (b) Angular profile of the $J=2-1$, 26.7-nm beam corresponding to the instant of its maximum. The beam peaks at $\approx 15$ mrad and its divergence is $\approx 10$ mrad. The larger data uncertainty compared to the $J=0-1$ case is due to partial overlapping of the two $J=2-1$ beams and their low intensity.

where it has been assumed that $g_f l \gg 1$ and $g_r l \gg 1$. The effective gain-length product in the half-cavity configuration is then

$$(gl)_{\text{eff}} \cong g_f l + g_r l + \ln R_{\text{eff}}. \tag{4}$$

The half cavity was produced in this work by a spherical x-ray Mo:Si multilayer mirror with a radius of curvature 130 mm. It comprised 12 layer pairs with a nominal period of 11.7 nm, deposited by ion-beam sputtering [56] upon a 25.4-mm-diam fused silica substrate with a rms surface roughness less than 1 Å. Its normal-incidence reflectivity $R$, measured with synchrotron radiation [57], was typically $\sim 30\%$ at the design 21.2-nm wavelength.

The basic requirement of the half-cavity design is that the radiation round-trip time in this device is smaller or at most equal to the gain lifetime. An analysis of the streak data reveals that the value $4.9\ \text{cm}^{-1}$ is maintained within $\pm 10\%$ over an $\sim 200$-ps interval, while a simple modeling based on the measured temporal shape of the ASE pulse provides an estimation of the FWHM gain lifetime of $\sim 280$ ps. This implies the maximal distance of the half-

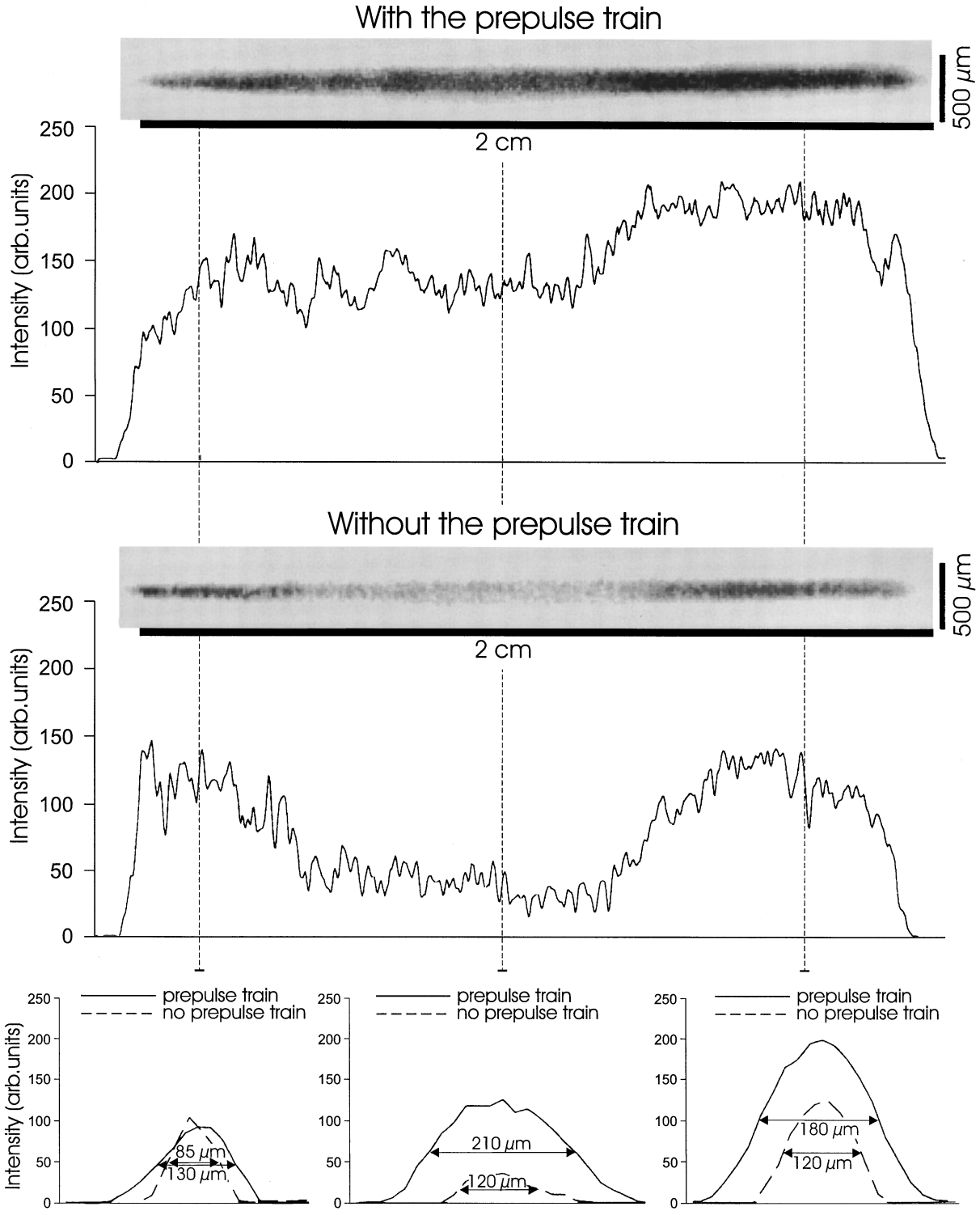


FIG. 10. Front-view images of a 2-cm-long zinc plasma in the keV spectral region, obtained with the multipinhole camera. The first record corresponds to the nominal prepulse train pumping regime, while the second was obtained when the main pulse alone was used. The densitometric traces taken down the plasma axis as well as perpendicular to it reveal that the prepulse pumping leads to an ≈60% increase of the lateral dimension of the keV-emitting region, to an axial uniformity improvement, and to an enhancement of the emitted signal.

cavity mirror from the end of a 2-cm plasma of about 10 mm. The XRM was therefore operated at a nominal distance of 9 mm, although a limited number of shots was carried out with the XRM positioned at 6 mm. In each case it was aligned to return the emission appearing at 7.2 mrad, i.e., corresponding to the beam angular peak, back along the same trajectory towards the amplifying region.

Given the measured $J=0-1$ gain region dimensions $30\times150$ $\mu$m$^2$ and the beam divergence $\sim3\times\sim7.5$ mrad$^2$ (a value corresponding to the geometric divergence is assumed in the latter case), by applying the ray optic approach and following Eq. (2) the effective reflectivity $R_{\text{eff}}$ for the XRM

placed at 9 mm amounts to $6.8\times10^{-2}$, while for the 6-mm distance we obtain $9.8\times10^{-2}$ [48]. Regarding the precision of knowledge of the individual parameters involved, we may expect conservatively that these calculated values apply in the real experiment with an accuracy of $\pm50\%$.

The radiation fed back by the XRM on the entrance plane of the gain region will be subjected to refraction and the total amplification received in the return pass will depend, among other things, on the injection angle and the divergence of the injected beam. However, in the studied laser, as discussed in Sec. III, amplification occurs along a narrowly defined, strongly gain-dominated ray path corresponding to the exit angle near 7.2 mrad, which undergoes only a minor temporal evolution during the duration of gain. By ensuring the ASE emission appearing at 7.2 mrad to reenter the gain region along the same trajectory after reflection on the XRM, the propagated gain $g_b$ may be assessed by the value $g_f$ measured for the single pass. Assuming, accordingly, $g_b=4.9\pm0.5\ \mathrm{cm}^{-1}$ and accounting for the calculated values of $R_{\mathrm{eff}}$, the effective gain-length product $(gl)_{\mathrm{eff}}$ achieved by double passing a 2-cm-long plasma by use of the half cavity with XRM at 9 mm will be $16.9^{+1.4}_{-1.7}$, whereas for the XRM at 6 mm it will reach $17.3^{+1.4}_{-1.7}$. These numbers suggest that the half-cavity output will, in both cases, exhibit saturation behavior and that the corresponding augmentation of intensity of emission produced by the double pass with respect to that of single pass will be lower than values indicated by Eq. (3) applying for the small-signal gain regime, namely, $\sim850$ and $\sim1250$ in the respective cases.

## V. HALF-CAVITY-GENERATED SATURATED OUTPUT AT 21.2 nm

The Mo:Si multilayer XRM was attached to a micromotor pad and was aligned by a telescope system, with a precision corresponding to the orientation of its normal better than $\pm0.5$ mrad in both the vertical and horizontal planes. It was protected from plasma debris by an independently positioned shield having a hole 1 mm in diameter to pass the x-ray laser beam. The mirror damage induced by a shot was thus restricted to a spot of typically less than 2 mm in diameter and each mirror could be used many times (typically $20\times$) without the necessity of realigning it between the shots. The x-ray laser beam was analyzed on the east side by using the same diagnostics suite as in the single-pass experiments and was properly attenuated by various Al filters so as to avoid saturation of the detector.

For the XRM operating at the distance of 9 mm, typically 60-fold enhancement of the time-integrated output signal compared to single pass is observed for a 2-cm-long plasma, with a very good reproducibility on the shot-to-shot basis. On the other hand, the enhancement brought by the XRM placed at the distance of 6 mm from a 2-cm plasma was $\sim80$. The temporal evolution of the half-cavity pulses generated in both configurations is shown in Fig. 11. It is seen that their shapes as well as their duration are similar to that of the single pass (Fig. 7), suggesting that no sudden destruction of the XRM structure occurs within the x-ray pulse duration. Equally it is seen that the ratio $\sim80/\sim60$ of the double-to-single-pass output augmentations for the two cases roughly equals the ratio of the corresponding $R_{\mathrm{eff}}$, which

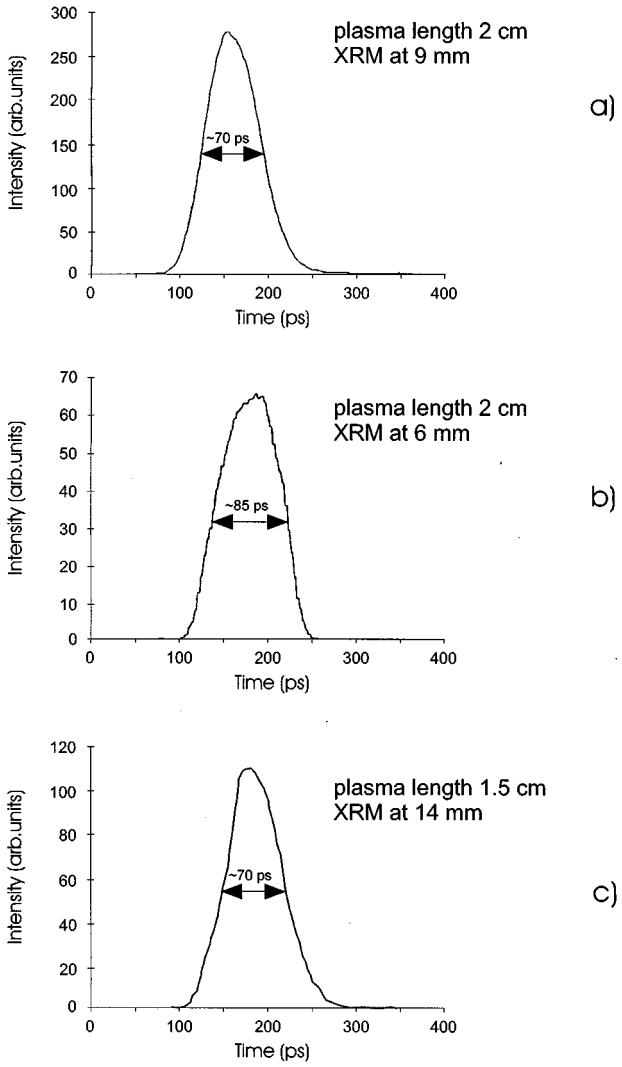


FIG. 11. Time-resolved 21.2-nm double-pass output produced by (a) a 2-cm plasma and the XRM placed at a distance of 9 mm, (b) a 2-cm plasma and the XRM placed at a distance of 6 mm, and (c) a 1.5-cm plasma and the XRM placed 14 mm from the plasma end. By comparing with Fig. 6 it is seen that both the FWHM duration and the overall character of the laser output are very similar to that produced in the single pass.

corroborates this observation and suggests that the estimations of effective reflectivities given above are basically correct.

To assess the magnitude of the small-signal return gain coefficient $g_r$ we examined a half-cavity configuration using a 1.5-cm-long plasma and the XRM positioned at 14 mm, in which the round-trip time is identical to that in the case of a 2-cm plasma and the XRM at the distance of 9 mm. As $R_{\mathrm{eff}}=4.5\times10^{-2}$ and assuming $g_r=4.9\pm0.5\ \mathrm{cm}^{-1}$, this setup should produce unsaturated output with $(gl)_{\mathrm{eff}}=11.6^{+1.2}_{-1.5}$ and should thus boost the output intensity by a factor of about 50. The time-integrated enhancement of the output signal [the temporal evolution of which is shown in Fig. 11(c)] with respect to the single-pass ASE generated by a 1.5-cm plasma is $\sim30$. This is fairly close to the expected value and suggests that a small-signal gain within the interval $4.9\pm0.5\ \mathrm{cm}^{-1}$ does exist during the return propagation of the x-ray beam in the half cavity using a 2-cm plasma.

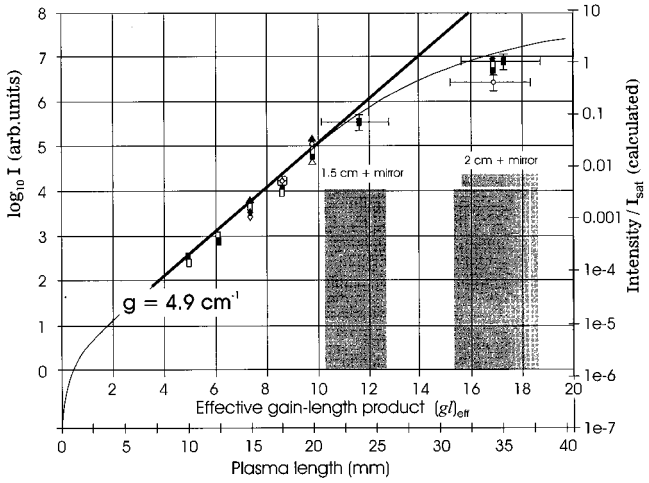


FIG. 12. Intensity of the $J=0-1$, 21.2-nm emission as a function of effective gain-length product $(gl)_{\mathrm{eff}}$, including data from both the single- and the double-pass shots (in $\log_{10}$ scale). The dashed line represents an exponential intensity increase with gain coefficient $g=4.9$ cm$^{-1}$. The $(gl)_{\mathrm{eff}}$ uncertainty for the half-cavity shots corresponds to the conservative error estimation of the efficient reflectivity $R_{\mathrm{eff}}$ and the gain $g_r$ present during the return pass (see the text). While the intensity rolloff from the exponential character for the half-cavity shots with a 2-cm plasma is clearly apparent, the solid curve represents the calculated dependence accounting for the effect of saturation (see the text). The right-hand scale corresponds to the calculated value of emitted-to-saturation intensity ratio.

The rolloff of the measured output from the exponential curve in that case occurs thus conclusively due to saturation.

An overview of the experimental results displaying the intensity of the x-ray laser as a function of the effective gain length is in Fig. 12. For the measurements obtained with the half cavity the gray column corresponds to the error in the gain-length estimation, arising from the assumed 50% accuracy of the calculated $R_{\mathrm{eff}}$ and from the considered interval 4.4–5.4 cm$^{-1}$ of the return gain coefficient $g_r$. The experimental data are compared to a curve obtained by a model calculation solving the equation of radiative transfer for the transition $(\frac{1}{2},\frac{1}{2})_{J=0}$ to $(\frac{1}{2},\frac{1}{2})_{J=1}$ and accounting for the rates of the processes involved in the kinetics of these levels [48] through their values provided by detailed numerical simulations [58,59]. It is seen that the calculated curve compares to the experimental data very well and confirms that the laser is saturated in the half-cavity shots with a 2-cm-long plasma.

The saturation intensity $I_{\mathrm{sat}}$ is defined (see, e.g., [60]) as the intensity reducing the small-signal gain by one-half and equals

$$I_{\mathrm{sat}}=\frac{h\nu}{\sigma\tau_R}, \tag{5}$$

where $h\nu$ is the photon energy, $\sigma=A\lambda^2/8\pi$ the cross section of stimulated emission ($A$ being the spontaneous emission rate), and $\tau_R$ the gain recovery time, which is determined by the processes *depopulating* the upper level $(\frac{1}{2},\frac{1}{2})_{J=0}$ in the small-signal regime. From the modeling we obtain $I_{\mathrm{sat}}=9.8\times10^9$ W/cm$^{-2}$ and taking into account the measured dimensions of the near-field pattern as well as the ~80-ps duration of the half-cavity emission, the energy of one pulse of the x-ray laser corresponding to the output intensity just equal to $I_{\mathrm{sat}}$ is estimated to ~170 $\mu$J.

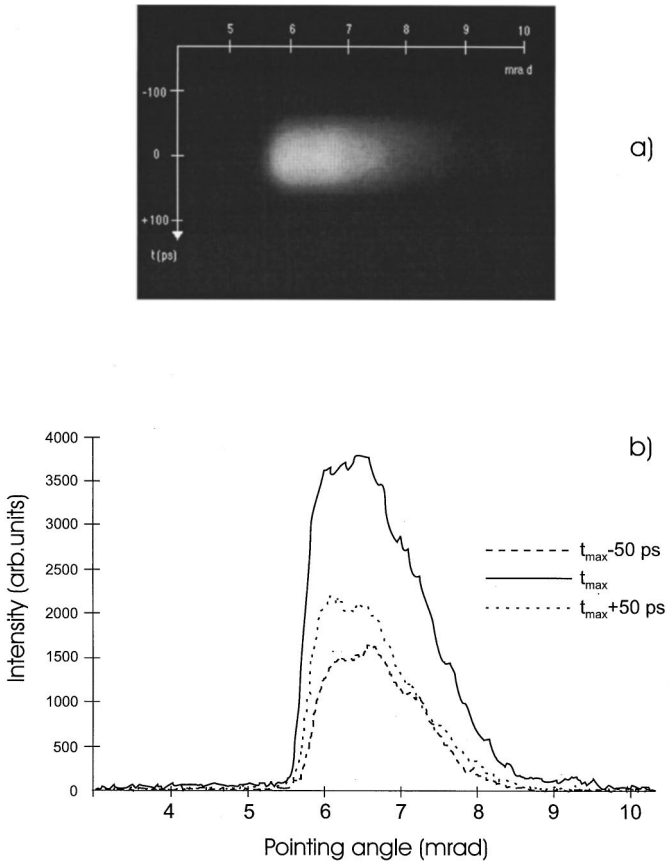


FIG. 13. Angular profile of the 21.2-nm beam emitted by a 2-cm plasma in the half-cavity configuration, in instants separated by 50 ps with respect to its maximum (the corresponding raw streak record is also provided). It is seen that the beam peaks near 6.3 mrad, which is slightly less than in the single-pass case (cf. Fig. 8), whereas the temporal evolution of this pointing angle is almost negligible.

The characteristics of the half-cavity-generated x-ray beam were investigated using the plane mirror and by recording its ''footprint'' on a CCD camera of calibrated spectral sensitivity. The horizontal angular profile of the double-pass emission generated by a 2-cm plasma, obtained with the help of the plane mirror, is shown in Fig. 13. The beam peaks at 6.3 mrad and its divergence is ~2.6 mrad, both values exhibiting only a negligible temporal evolution. From the comparison with the single-pass profile it is seen that although the half-cavity beam exhibits a slightly reduced divergence as well as the refraction angle, the profiles are alike, suggesting that the return amplification occurs along a ray path that is similar to the one in the case of a single pass.

The energy of the x-ray beam was obtained from footprint shots performed in two separate experiments using thinned backside-illuminated CCD cameras Thomson 512×512 pixel TSC 7395A and Tektronix 1024×1024 pixel-type, respectively. The x-ray beam was properly bandpassed and relayed onto the CCD chip by a 21.2-nm Mo:Si multilayer optics of measured reflectance. In one case a single 45°-angle-of-incidence multilayer mirror was used, while a set of

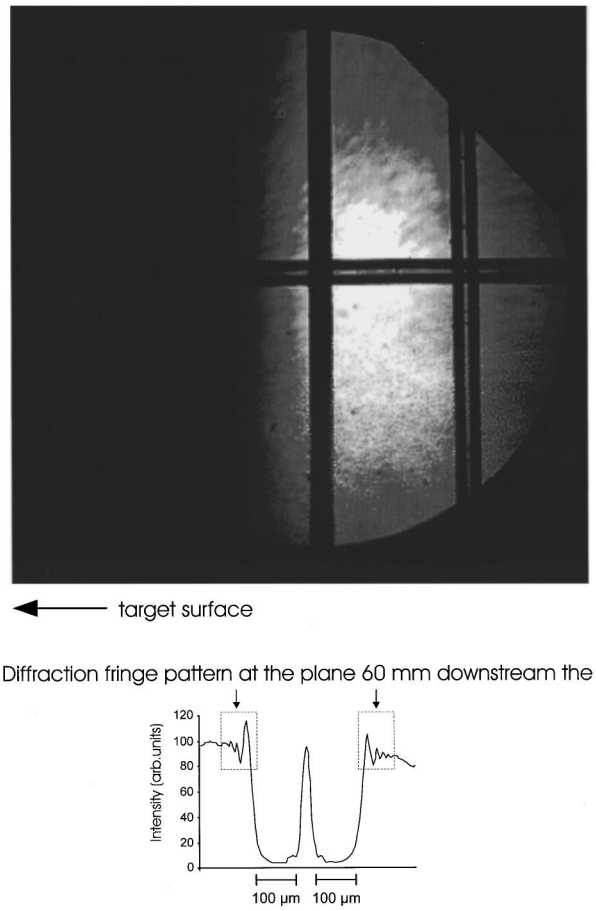


FIG. 14. Footprint image of the half-cavity generated 21.2-nm beam after passing a cross-wire system placed at a distance of 50 cm from the plasma, revealing a $2.8\times6$ mrad$^2$ time-integrated profile. The 100-$\mu$m-diam wires are separated by 1 mm. The diffraction fringe patterns shown are produced on the wire edges and correspond to the distance of 60 mm downstream the cross-wire system.

three mirrors was employed in another case (the details about both arrangements may be found elsewhere [13,48]).

The measurements provided an energy of typically 0.4 mJ, which corresponds to $4\times10^{13}$ photons, in one half-cavity pulse. A footprint image of the half-cavity-generated beam is shown in Fig. 14. The record corresponds to the beam intensity distribution at the distance of about 50 cm from the plasma exit, 6 cm downstream a reference cross-wire system attached on a 5-mm-diam aperture. While the record provides a beam with the divergence of about $2.8\times6$ mrad$^2$ in the horizontal and vertical directions, it supplies also basic information about the beam transverse coherence through diffraction fringes present at the edges of the wire shadow. As seen from Fig. 14, typically four fringes are thus observed, from which we infer a transverse coherence length of $\sim45$ $\mu$m [48].

Combined with the $\sim80$-ps half-cavity pulse duration, the energy of 0.4 mJ gives a peak output power of $\sim5$ MW. Regarding the $35\times150$ $\mu$m$^2$ output aperture, the brightness amounts to $\sim3\times10^{15}$ W cm$^{-2}$ sr$^{-1}$ per bandwidth of 0.01% of the emitting 21.2-nm wavelength, which makes this laser one of the brightest laboratory soft-x-ray sources developed thus far.

## VI. CONCLUSIONS AND PROSPECTS

In this paper we described the neonlike zinc soft-x-ray laser operating at 21.2 nm, which has been developed at the LSAI and LULI. A summary of the major characteristics of this laser and of its driver is displayed in Table I.

While in the single-pass ASE regime the laser delivers 5–7 $\mu$J, the full 0.4 mJ energy per pulse quoted in Table I is achieved by employing the half-cavity configuration. It should be noted that despite operating the half-cavity x-ray multilayer mirror in the close proximity to the plasma, the mirror damage has not been found to be a limiting factor in the design of this soft-x-ray laser and the half-cavity shots are now routinely performed.

The 21.2-nm laser described has been experimentally characterized in many parameters. Its functioning relies essentially on the use of the prepulse-train pumping and also, although to a lesser extent, on the creation of an acceptably uniform irradiation along the focus axis. It should be noted that the influence of very weak prepulses on parameters of the laser plasma presents a relatively new topic in the laser-plasma physics—especially in the context of collisionally pumped x-ray lasers—with some aspects neither experimentally nor theoretically fully resolved. Regarding the key importance of prepulses for the studied zinc laser, we have been expending some effort on the investigation of this issue. The analysis of the near- and far-field patterns of the lasing lines provide strong evidence for an increase of the transverse (perpendicular to the target) plasma scale length in the prepulse regime, confirming the results of computer simulations predicting such an effect. The obtained data also suggest that the prepulse pumping leads to an increase of the active plasma and thereby equally to an increase of the lateral plasma scale length.

We have recently undertaken several experiments using single prepulses arriving 2 and 4.5 ns ahead of the main pulse, devoted to a detailed investigation of the dependence of the $J=0-1$ output in Zn ($Z=30$), Cu ($Z=29$), and Ni ($Z=28$) on the prepulse contrast ratio and delay [38,48]. The major finding is that Zn exhibits rather unique behavior, namely, that with the 4.5-ns delay there is a contrast ratio (energy of the prepulse vs the energy of the main pulse) of $\sim2\times10^{-3}$ for which the maximal $J=0-1$ output is generated, while for Cu and Ni the $J=0-1$ signal increases monotonically with the prepulse level, as it does for all three elements when the 2-ns delay is used. This result suggests that the prepulse effect is critically dependent on the solid-state properties of the given element and that their exact description is crucial to theoretically reproduce the observed behavior. This has not yet been achieved, as the computer simulations predict a $J=0-1$ output increase with increasing prepulse contrast ratio. We note that in another work [47] the largest $J=0-1$ output was produced at a contrast ratio of $\sim0.02$ using a prepulse applied 5 ns ahead of the main pulse, the irradiance supplied by the latter of $3\times10^{13}$ W cm$^{-2}$ being, however, higher than in our studies. Obviously further effort, including the investigation of the preplasma alone, is to be spent to achieve a full understanding of this phenomenon. We note that experimental studies devoted to investigation of Zn and Cu plasmas created by intensities in the range $10^9-10^{11}$ W cm$^{-2}$ [39], i.e., pertinent to those created

TABLE I. Characteristics of the 21.2-nm zinc soft-x-ray laser in the half-cavity configuration. BW denotes bandwidth.

| | |
|---|---|
| Driving wavelength | 1.06 $\mu$m |
| Net driving energy | $\sim$350 J |
| Energy of the last prepulse in the prepulse train | $\approx$170 mJ |
| Net driving intensity | $\sim 1.4\times 10^{13}$ W cm$^{-2}$ |
| XRL wavelength | 21.22 nm |
| Energy in the XRL beam | 0.4 mJ |
| Number of photons in the XRL beam | $4\times 10^{13}$ |
| XRL pulse duration | 80 ps |
| XRL beam peak power | 5 MW |
| XRL beam solid angle | $2.5\times 10^{-5}$ sr |
| XRL brightness | $3\times 10^{15}$ W cm$^{-2}$ sr$^{-1}$ (0.01 BW)$^{-1}$ |
| Transverse coherence length (50 cm from the plasma) | 45 $\mu$m |
| Efficiency (XRL energy/driving energy) | $10^{-6}$ |
| Efficiency (gl/TW of driving energy) | 24 TW$^{-1}$ |
| Repetition rate | 1 shot/20 min |

by the prepulses discussed here, reveal strong differences of the plasma parameters between these two elements.

As concerns the studied zinc soft-x-ray laser, using the prepulse train has lead to the largest 21.2-nm output. However, no definitive conclusion can be made at this point as the maximal delay of the single pulse was 4.5 ns compared to the 10-ns prepulse separation in the train, although we note that generating the prepulse train is conceptually simple as this is naturally produced by mode-locked oscillators. By changing the extinction ratio of the Pockels cell used under normal circumstances to isolate the prepulse train from the main pulse, the intensity of the prepulse train may be varied. However, in general, the laser chain may amplify pulses of different intensities in a nonlinear way. To exploit this approach in a manageable fashion, it is therefore necessary to have a fast response energy monitor to record the final energy on target from each pulse.

At present, the 21.2-nm zinc laser is further optimized and is exploited as a tool for applications of soft-x-ray radiation. Studies of curved targets in the half-cavity configuration have been initiated and the early measurements indicate that this arrangement is able to boost the output energy to a millijoule level [61]. Experiments using different half-cavity configurations, with the aim to improve the transverse coherence, are equally planned. In parallel, systematic investigation of the prepulse effect is being pursued. Concerning the applications, two main topics are currently being developed. Studies of UV soft-x-ray excited luminescence of some halogenide crystals such as CsI and CsCl have been made [20]. Experiments to use the 21.2-nm soft-x-ray beam to probe high-density plasmas through interferometry techniques are in preparation.

## ACKNOWLEDGMENTS

The multilayer mirrors used in these experiments were designed and fabricated by J. P. Chauvineau and his team of the Institut d'Optique Théorique et Appliquée in Orsay and were tested for reflectivity with synchrotron radiation by T. Lucatorto, C. Tarrio, and R. Watts of the NIST Physics Laboratory, Gaithersburg. Their work is greatly appreciated. We are grateful to Daniel Mazataud and Alain Mens of CEA Limeil and to Dennis Matthews, Luiz da Silva, and Bob Cauble of LLNL for providing the thinned absolutely calibrated CCD cameras that were used in the x-ray beam energy measurements. We gratefully acknowledge excellent technical support of Jean Claude Lagron and Laurent Vanbostal, as well as the effort of LULI laser facility staff. Finally, we would like to thank Alain Sureau of LSAI, Sylvie Jacquemot of CEA Limeil, and Phil Holden of LSAI for many valuable discussions on various theoretical issues.

[1] D. L. Matthews, P. L. Hagelstein, M. D. Rosen, M. J. Eckart, N. M. Ceglio, A. U. Hazi, H. Medecki, B. J. MacGowan, J. E. Trebes, B. L. Whitten, E. M. Campbell, C. W. Hatcher, J. H. Scofield, G. Stone, and T. A. Weaver, Phys. Rev. Lett. **54**, 110 (1985).

[2] B. J. MacGowan, L. B. DaSilva, D. J. Fields, C. J. Keane, J. A. Koch, R. A. London, D. L. Matthews, S. Maxon, S. Mrowka, A. L. Osterheld, J. H. Scofield, G. Shimkaveg, J. E. Trebes, and R. S. Walling, Phys. Fluids. B **4**, 2326 (1992).

[3] *Proceedings of the Fourth International Colloquium on X-Ray Lasers*, edited by D. C. Eder and D. L. Matthews, AIP Conf. Proc. No. 332 (AIP, New York, 1994).

[4] J. J. Rocca, V. N. Shlyaptsev, F. G. Tomasel, O. D. Cortazar, D. Hartshorn, and J. L. A. Chilla, Phys. Rev. Lett. **73**, 2192 (1994).

[5] D. C. Eder, P. Amendt, and S. C. Wilks, Phys. Rev. A **45**, 6761 (1992).

[6] S. Maxon, K. G. Estabrook, M. K. Prasad, A. L. Osterheld, R. A. London, and D. C. Eder, Phys. Rev. Lett. **70**, 2285 (1993).

[7] A. McPherson, T. S. Luk, B. D. Thompson, K. Boyer, and C. K. Rhodes, Appl. Phys. B **57**, 337 (1993).

[8] P. A. Loboda, V. Lykov, V. Y. Politov, and J. Nilsen, Appl.

Phys. B **57**, 325 (1993).
[8] Y. Nagata, K. Midorikawa, S. Kubodera, M. Obara, H. Tashiro, and K. Toyoda, Phys. Rev. Lett. **71**, 3774 (1993).
[9] S. J. Moon, D. C. Eder, and G. L. Ströbel, in *Proceedings of the Fourth International Colloquium on X-Ray Lasers* (Ref. [3]), pp. 262–266.
[10] J. Zhang, M. H. Key, S. J. Rose, and G. J. Tallents, Phys. Rev. A **49**, 4024 (1994).
[11] B. E. Lemoff, G. Y. Yin, C. L. Gordon III, C. P. Barty, and S. E. Harris, Phys. Rev. Lett. **74**, 1574 (1995).
[12] P. Jaeglé, A. Carillon, P. Dhez, P. Goedtkindt, G. Jamelot, A. Klisnick, B. Rus, P. Zeitoun, S. Jacquemot, D. Mazataud, A. Mens, and J. P. Chauvineau, in *Proceedings of the Fourth International Colloquium on X-Ray Lasers* (Ref. [3]), pp. 25–34.
[13] G. Jamelot, P. Jaeglé, B. Rus, A. Carillon, A. Klisnick, M. Nantel, S. Sebban, F. Albert, P. Zeitoun, E. Planckl, A. Sirgand, C. L. S. Lewis, A. MacPhee, G. J. Tallents, J. Krishnan, and M. Holden, SPIE Proc. **2520**, 2 (1995).
[14] G. J. Tallents, P. Zeitoun, A. Behjat, A. Demir, M. Holden, J. Krishnan, C. L. S. Lewis, A. MacPhee, P. J. Warwick, M. Nantel, G. Jamelot, B. Rus, P. Jaeglé, A. Klisnick, P. Goedtkindt, A. Carillon, E. E. Fill, Y. Li, G. Pretzler, D. Schlögl, J. Steingruber, D. Neely, P. Norreys, M. H. Key, J. Zhang, G. J. Pert, P. Holden, and J. Plowes, SPIE Proc. **2520**, 34 (1995).
[15] A. Carillon, H. Z. Chen, P. Dhez, L. Dwivedi, J. Jacoby, P. Jaeglé, G. Jamelot, J. Zhang, M. H. Key, A. Kidd, A. Klisnick, R. Kodama, J. Krishnan, C. L. S. Lewis, D. Neely, P. Norreys, D. M. O'Neill, G. J. Pert, S. A. Ramsden, J. P. Raucourt, G. J. Tallents, and J. Uhomoibhi, Phys. Rev. Lett. **68**, 2917 (1992).
[16] L. B. Da Silva, R. A. London, B. J. MacGowan, S. Mrowka, and D. L. Matthews, Opt. Lett. **19**, 1532 (1994).
[17] B. Rus, C. L. S. Lewis, G. F. Cairns, P. Dhez, P. Jaeglé, M. H. Key, D. Neely, A. G. MacPhee, S. A. Ramsden, C. G. Smith, and A. Sureau, Phys. Rev. A **51**, 2316 (1995).
[18] L. B. Da Silva, T. W. Barbee, R. Cauble, P. Celliers, J. Harder, H. R. Lee, R. A. London, D. L. Matthews, S. Mrowka, J. C. Moreno, D. Ress, J. E. Trebes, A. Wan, and F. Weber, Rev. Sci. Instrum. **66**, 574 (1995).
[19] P. Jaeglé, S. Sebban, A. Carillon, G. Jamelot, A. Klisnick, P. Zeitoun, B. Rus, M. Nantel, F. Albert, and D. Ros, J. Appl. Phys. (to be published).
[20] R. R. Haar, L. J. Curtis, N. Reistad, C. Jupén, I. Martinson, B. M. Johnson, K. W. Jones, and M. Meron, Phys. Scr. **35**, 296 (1987).
[21] G. D. Enright, D. M. Villeneuve, J. Dunn, H. A. Baldis, J. C. Kieffer, H. Pépin, M. Chaker, and P. R. Herman, J. Opt. Soc. Am. B **8**, 2047 (1991).
[22] M. Nantel, J. C. Kieffer, B. LaFontaine, H. Pépin, G. D. Enright, D. M. Villeneuve, J. Dunn, H. A. Baldis, and O. Peyrusse, Phys. Fluids B **5**, 4465 (1993).
[23] E. E. Fill, Y. Li, P. X. Lu, and G. Pretzler, in *X-Ray Lasers 1996*, edited by S. Svanberg and C.-G. Wahlström, IOP Conf. Proc. No. 151 (Institute of Physics and Physical Society, London, 1996), pp. 25–31.
[24] H. Fiedorowicz, A. Bartnik, Y. Li, P. Lu, and E. Fill, Phys. Rev. Lett. **76**, 415 (1996).
[25] D. J. Fields, R. S. Walling, G. M. Shimkaveg, B. J. MacGowan, L. B. Da Silva, J. H. Scofield, A. L. Osterheld, T. W. Phillips, M. D. Rosen, D. L. Matthews, W. H. Goldstein, and R. E. Stewart, Phys. Rev. A **46**, 1606 (1992).
[26] G. M. Shimkaveg, M. R. Carter, R. S. Walling, J. M. Ticehurst, R. A. London, and R. E. Stewart, in *X-Ray Lasers 1992*, edited by E. E. Fill, IOP Conf. Proc. No. 125 (Institute of Physics and Physical Society, London, 1992), pp. 61–66.
[27] R. E. Marrs, M. A. Levine, D. A. Knapp, and J. R. Henderson, Phys. Rev. Lett. **60**, 1715 (1988).
[28] S. R. Elliot, P. Beiersdorfer, and J. Nilsen, in *Proceedings of the Fourth International Colloquium on X-Ray Lasers* (Ref. [3]), pp. 307–311.
[29] J. Nilsen, J. C. Moreno, B. J. MacGowan, and J. A. Koch, Appl. Phys. B **57**, 309 (1993).
[30] J. Nilsen, B. J. MacGowan, L. B. DaSilva, and J. C. Moreno, Phys. Rev. A **48**, 4682 (1993).
[31] G. F. Cairns, M. J. Lamb, C. L. S. Lewis, A. G. MacPhee, D. Neely, P. Norreys, M. H. Key, C. Smith, S. B. Healy, P. B. Holden, G. Pert, and J. A. Plowes, in *Proceedings of the Fourth International Colloquium on X-Ray Lasers* (Ref. [3]), pp. 289–292.
[32] G. F. Cairns, C. L. S. Lewis, M. J. Lamb, A. G. MacPhee, D. Neely, P. Norreys, M. H. Key, S. B. Healy, P. B. Holden, G. J. Pert, J. A. Plowes, G. J. Tallents, and A. Demir, Opt. Commun. **123**, 777 (1996).
[33] J. C. Moreno, J. Nilsen, and L. B. DaSilva, Opt. Commun. **110**, 585 (1994).
[34] H. Daido, R. Kodama, K. Murai, G. Yuan, M. Takagi, Y. Kato, I. W. Choi, and C. H. Nam, Opt. Lett. **20**, 61 (1995).
[35] M. Nantel, A. Klisnick, G. Jamelot, P. B. Holden, P. Jaeglé, P. Zeitoun, G. Tallents, A. G. MacPhee, and C. L. S. Lewis, Opt. Lett. **20**, 2333 (1995).
[36] M. Nantel, A. Klisnick, G. Jamelot, P. B. Holden, P. Jaeglé, B. Rus, P. Zeitoun, G. Tallents, A. G. MacPhee, C. L. S. Lewis, S. Jacquemot, and L. Bonnet, Phys. Rev. E **54**, 2852 (1996).
[37] A. G. MacPhee, C. L. S. Lewis, P. J. Warwick, I. Weaver, A. Demir, M. Holden, J. Krishnan, G. J. Tallents, P. Goedtkindt, P. Jaeglé, G. Jamelot, A. Klisnick, M. Nantel, B. Rus, and P. Zeitoun, Opt. Commun. **133**. 525 (1997).
[38] B. Rus, P. Zeitoun, T. Mocek, S. Sebban, M. Kalal, A. Demir, G. Jamelot, A. Klisnick, G. J. Tallents, in *X-Ray Lasers 1996* (Ref. [24]), pp. 394–398.
[39] S. Jacquemot and L. Bonnet, SPIE Proc. **2520**, 169 (1995).
[40] S. B. Healy, G. F. Cairns, C. L. S. Lewis, G. J. Pert, and J. A. Plowes, IEEE Sel. Top. Quantum Electron. **1**, 949 (1995).
[41] R. Kodama, D. Neely, Y. Kato, H. Daido, K. Murai, G. Yuan, A. MacPhee, and C. L. S. Lewis, Phys. Rev. Lett. **73**, 3215 (1994).
[42] Y. Kato, R. Kodama, H. Daido, K. Murai, G. Yuan, S. Ninomiya, D. Neely, A. MacPhee, C. L. S. Lewis, I. W. Choi, C. H. Nam, and T. Kawachi, in *Proceedings of the Fourth International Colloquium on X-Ray Lasers* (Ref. [3]), pp. 35–40.
[43] J. Nilsen, Y. Li, P. Lu, J. C. Moreno, and E. E. Fill, Opt. Commun. **124**, 287 (1996).
[44] B. Rus, A. Carillon, B. Gauthé, P. Goedtkindt, P. Jaeglé, G. Jamelot, A. Klisnick, A. Sureau, and P. Zeitoun, J. Opt. Soc. Am. B. **11**, 546 (1994).
[45] B. Rus, A. Carillon, P. Dhez, B. Gauthé, P. Goedtkindt, P. Jaeglé, G. Jamelot, A. Klisnick, M. Nantel, A. Sureau, and P. Zeitoun, in *Proceedings of the Fourth International Colloquium on X-Ray Lasers* (Ref. [3]), pp. 152–156.

[47] E. E. Fill, Y. Li, D. Schlögl, J. Steingruber, and J. Nilsen, Opt. Lett. **20**, 374 (1995).
[48] B. Rus, Ph.D. thesis, Université Paris–Sud, 1995 (unpublished).
[49] Y. Kato, H. Daido, H. Shiraga, M. Yamanaka, H. Azuma, K. Murai, E. Miura, G. Yuan, M. Ohmi, K. Tanaka, T. Kanabe, M. Tagaki, S. Nakai, C. L. S. Lewis, D. M. O'Neill, D. Neely, K. Shimohara, M. Niibe, and Y. Fukuda, SPIE Proc. **1551**, 56 (1991).
[50] A. Carillon, P. Dhez, B. Gauthé, P. Jaeglé, G. Jamelot, A. Klisnick, and J. C. Lagron, SPIE Proc. **1140**, 271 (1989).
[51] P. Dhez, A. Carillon, F. Wuilleumier, E. Kälne, V. Schmidt, and M. Berland, Nucl. Instrum. Methods **152**, 85 (1978).
[52] B. Rus, P. Zeitoun, A. Carillon, B. Gauthé, P. Jaeglé, G. Jamelot, A. Klisnick, J. C. Lagron, and C. Vinsot, in *X-Ray Lasers 1992* (Ref. [27]), pp. 361–366.
[53] G. J. Linford, E. R. Peressini, W. R. Sooy, and M. L. Spaeth, Appl. Opt. **13**, 379 (1974).
[54] P. B. Holden and B. Rus, Opt. Commun. **119**, 424 (1995).
[55] P. B. Holden, S. B. Healy, M. T. M. Lightbody, G. J. Pert, J. A. Plowes, A. E. Kingston, E. Robertson, C. L. S. Lewis, and D. Neely, J. Phys. B **27**, 341 (1994).
[56] J. P. Chauvineau (private communication).
[57] T. Lucatorto, C. Tarrio, and R. Watts (private communication).
[58] P. B. Holden (private communication).
[59] S. Jacquemot (private communication).
[60] A. Yariv, *Quantum Electronics*, 3rd ed. (Wiley, New York, 1989).
[61] P. Jaeglé, S. Sebban, A. Carillon, G. Jamelot, A. Klisnick, P. Zeitoun, B. Rus, F. Albert, and D. Ros, in *X-Ray Lasers 1996* (Ref. [24]), pp. 528–532.